A&A 667, A64 (2022)
https://doi.org/10.1051/0004-6361/202244186

Astronomy & Astrophysics

Brown dwarf companions in microlensing binaries detected during the 2016–2018 seasons

Cheongho Han[1], Yoon-Hyun Ryu[2], In-Gu Shin[1], Youn Kil Jung[2], Doeon Kim[1], Yuki Hirao[3], Valerio Bozza[4,5], Michael D. Albrow[6], Weicheng Zang[7], Andrzej Udalski[8], Ian A. Bond[9], Sun-Ju Chung[2], Andrew Gould[10,11], Kyu-Ha Hwang[2], Yossi Shvartzvald[12], Hongjing Yang[7], Sang-Mok Cha[2,13], Dong-Jin Kim[2], Hyoun-Woo Kim[2], Seung-Lee Kim[2], Chung-Uk Lee[2], Dong-Joo Lee[2], Jennifer C. Yee[15], Yongseok Lee[2,14], Byeong-Gon Park[2,14], Richard W. Pogge[11]
(The KMTNet Collaboration)
Przemek Mróz[8], Michał K. Szymański[8], Jan Skowron[8], Radek Poleski[8], Igor Soszyński[8], Paweł Pietrukowicz[8], Szymon Kozłowski[8], Krzysztof Ulaczyk[16], Krzysztof A. Rybicki[8,12], Patryk Iwanek[8], Marcin Wrona[8]
(The OGLE Collaboration)
Fumio Abe[17], Richard Barry[18], David P. Bennett[18,19], Aparna Bhattacharya[18,19], Hirosame Fujii[17], Akihiko Fukui[20,21], Stela Ishitani Silva[18,22], Rintaro Kirikawa[3], Iona Kondo[3], Naoki Koshimoto[23], Yutaka Matsubara[17], Sho Matsumoto[3], Shota Miyazaki[3], Yasushi Muraki[17], Arisa Okamura[3], Greg Olmschenk[18], Clément Ranc[24], Nicholas J. Rattenbury[25], Yuki Satoh[3], Takahiro Sumi[3], Daisuke Suzuki[3], Taiga Toda[3], Paul J. Tristram[26], Aikaterini Vandorou[18,19], Hibiki Yama[3], and Yoshitaka Itow[17]
(The MOA Collaboration)

(Affiliations can be found after the references)

Received 4 June 2022 / Accepted 8 September 2022

ABSTRACT

Aims. With the aim of finding microlensing binaries containing brown dwarf (BD) companions, we investigate the microlensing survey data collected during the 2016–2018 seasons.
Methods. For this purpose, we first modeled lensing events with light curves exhibiting anomaly features that are likely to be produced by binary lenses. We then sorted out BD companion binary-lens events by applying the criterion that the companion-to-primary mass ratio is $q \lesssim 0.1$. With this procedure, we identify six binaries with candidate BD companions: OGLE-2016-BLG-0890L, MOA-2017-BLG-477L, OGLE-2017-BLG-0614L, KMT-2018-BLG-0357L, OGLE-2018-BLG-1489L, and OGLE-2018-BLG-0360L.
Results. We estimated the masses of the binary companions by conducting Bayesian analyses using the observables of the individual lensing events. According to the Bayesian estimation of the lens masses, the probabilities for the lens companions of the events OGLE-2016-BLG-0890, OGLE-2017-BLG-0614, OGLE-2018-BLG-1489, and OGLE-2018-BLG-0360 to be in the BD mass regime are very high with $P_{\rm BD} > 80\%$. For MOA-2017-BLG-477 and KMT-2018-BLG-0357, the probabilities are relatively low with $P_{\rm BD} = 61\%$ and 69%, respectively.

Key words. gravitational lensing: micro – brown dwarfs

1. Introduction

One important scientific feature of microlensing is its capability of detecting faint or dark objects. For this reason, a microlensing experiment was originally proposed to search for dark matter in the form of massive compact halo objects lying in the Galactic halo (Paczyński 1986). Since the completion of the first-generation experiments conducted for this purpose, for example, MACHO (Alcock et al. 1996), EROS (Aubourg et al. 1995), and OGLE (Udalski et al. 1993), the application of microlensing was expanded to looking for faint binary companions to stars (Mao & Paczyński 1991), including planets and brown dwarfs (BDs). At the time of writing this paper, 173 microlensing planets were reported according to the Extrasolar Planets Encyclopaedia[1]. The list of microlensing BDs is given in Table 1 of Chung et al. (2019), which includes 18 BDs, in addition to which, 9 BDs or candidates have been reported since that time (Shvartzvald et al. 2019; Jung et al. 2018; Miyazaki et al. 2018; Han et al. 2020a,b; Herald et al. 2022).

The microlensing signature of a planet, with a planet-to-host mass ratio of about 10^{-3} or lower, can in most cases be readily identified from its characteristic signature of a short-term anomaly to the lensing light curve produced by the host of the planet (Gould & Loeb 1992). By contrast, an immediate identification of a BD companion belonging to a binary lens is generally much more difficult because the lensing light curve produced by a binary containing a BD companion, with a mass ratio of the BD companion to its primary of about 10^{-2}, is not much different from those produced by binaries composed of roughly equal-mass components, and thus it does not usually exhibit a characteristic pattern that would enable one to immediately

[1] http://exoplanet.eu/

Table 1. ID references, alert dates, and coordinates of lensing events.

KMTNet	OGLE	MOA	$(RA, Dec)_{J2000}$ (l, b)
KMT-2016-BLG-0793 (postseason)	**OGLE-2016-BLG-0890** (0934) (2016-05-18)		(17:30:25.69, −29:50:48.98) (−2°.540, 2°.308)
KMT-2017-BLG-1757 (postseason)		**MOA-2017-BLG-477** (2017-09-15)	(18:05:50.00, −27:04:38.50) (3°.854, −2°.918)
KMT-2017-BLG-2209 (postseason)	**OGLE-2017-BLG-0614** (2017-04-23)		(17:26:08.08, −30:17:46.14) (−3°.430, 2°.833)
KMT-2018-BLG-0357 (2018-06-30)			(17:44:12.20, −33:36:23.18) (−4°.143, 2°.180),
KMT-2018-BLG-1534 (postseason)	**OGLE-2018-BLG-1489** (2018-08-12)		(17:45:46.60, −23:57:43.85) (4°.267, 2°.559)
KMT-2018-BLG-2014 (postseason)	**OGLE-2018-BLG-0360** (2018-03-15)	MOA-2018-116 (2018-04-22)	(17:52:01.26, −31:08:54.71) (1°.183, −2°.326)

identify the existence of a BD companion[2]. This implies that identifying binaries with BD companions requires modeling all the lensing light curves of more than a hundred binary lensing events that are annually detected by the current lensing surveys. As we discussed below, binary-lens modeling requires heavy computations not only because of the large number of parameters required to be included in the modeling, but also because of the need to employ numerical methods.

With the aim of finding binaries containing BD companions, we investigated the microlensing survey data. In this paper, we report six binaries with candidate BD companions found from investigating the three years of microlensing data obtained during the seasons from 2016 to 2018: OGLE-2016-BLG-0890L, MOA-2017-BLG-477L, OGLE-2017-BLG-0614L, KMT-2018-BLG-0357L, OGLE-2018-BLG-1489L, and OGLE-2018-BLG-0360L.

For the presentation of the work, we arrange the paper according to the following organization. In Sect. 2 we describe the data used in the analysis, the instruments used for the acquisition of the data, and the procedure of data reduction. In Sect. 3 we mention the procedure of modeling lensing light curves and the criteria we applied to sort out BD companion binary-lens events. In Sects. 3.1–3.6, we explain the details of the modeling we conducted for the individual lensing events, and present the lensing parameters and configurations of the lens systems. In Sect. 4 we specify the source stars, measure their angular radii, and estimate the Einstein radii of the individual events. In Sect. 5 we estimate the physical parameters of the lenses, including the masses of the binary components and distances to the lens systems. In Sect. 6 we summarize the results found from the analyses and conclude.

2. Observations and data

For the searches of BD events, we first investigated the data of the Korea Microlensing Telescope Network (KMTNet: Kim et al. 2016) survey that were collected during the first three years of its full operation from 2016 to 2018. During these seasons, 2588, 2817, and 2781 lensing events were found by the KMTNet survey in the 2016, 2017, and 2018 seasons, respectively. Among these events, we conducted systematic analyses of anomalous events, for which lensing light curves exhibited deviations from the form of single-lens single-source (1L1S) events (Paczyński 1986). Analyses conducted for the individual events vary depending on the nature of the anomalies, for example, planetary (Han et al. 2020c), binary-lens (Han et al. 2019), binary-source (Jung et al. 2017), triple-lens (Han et al. 2022), and binary-lens binary-source (Han et al. 2021a) modeling, and details of the analyses for different types of anomalies are described in the cited references. For candidate BD events found from this investigation, we conducted detailed analyses using improved data processed from optimized photometry of the events. We then confirmed whether the events were additionally observed by the two other working lensing surveys of the Optical Gravitational Lensing Experiment (OGLE; Udalski et al. 2015) and the Microlensing Observations in Astrophysics survey (MOA; Bond et al. 2001) in order to include these additional data in the analyses.

From the investigation, we found six candidate BD binary events: KMT-2016-BLG-0793/OGLE-2016-BLG-0934, KMT-2017-BLG-1757/MOA-2017-BLG-477, KMT-2018-BLG-1534/OGLE-2018-BLG-1489, KMT-2018-BLG-0357, KMT-2018-BLG-1534/OGLE-2018-BLG-1489, and KMT-2018-BLG-2014/OGLE-2018-BLG-0360/MOA-2018-BLG-116. Four of these events were observed by two surveys, one was observed by all the three surveys, and one was observed solely by the KMTNet survey. In Table 1 we summarize the ID references of the events assigned by the individual survey groups together with the alert dates and coordinates. This paper is the first release of BD events found from the systematic investigation of the KMTNet data collected during 2016–2018 seasons, and we plan to search for more BD events by investigating the data of the subsequent seasons.

For the events observed by multiple surveys, we hereafter use the ID references of the first discovery surveys, marked in bold font in Table 1, for the designation of the events. The notation "postseason" for the KMTNet events indicates that the events were found from the postseason investigation of the data (Kim et al. 2018b). We note that OGLE and MOA lensing events were found in real time with the progress of the events during the 2016–2018 seasons, but the real-time alert by the KMTNet survey, the AlertFinder algorithm (Kim et al. 2018a), has been operated since the 2018 season. There are two ID references for OGLE-2016-BLG-0890 (the other being OGLE-2016-BLG

[2] A lensing event produced by a giant planet lying at around the Einstein ring of the host also results in a lensing light curve with a planet signal that significantly deviates from a short-term anomaly (Han et al. 2021b).

-0934) because the source of the event was located in two OGLE fields. In this case, we used both data sets.

Observations by the KMTNet survey were carried out by employing three identical telescopes, each of which has a 1.6 m aperture. The KMTNet telescopes are globally distributed in three continents of the Southern Hemisphere, and the sites of the individual telescopes are the Siding Spring Observatory in Australia (KMTA), the Cerro Tololo Interamerican Observatory in Chile (KMTC), and the South African Astronomical Observatory in South Africa (KMTS). The telescopes used by the OGLE and MOA surveys are located at the Las Campanas Observatory in Chile and the Mt. John Observatory in New Zealand, respectively, and the individual telescopes have 1.3 m and 1.8 m apertures. The KMTNet, OGLE, and MOA telescopes are equipped with cameras yielding 4 deg^2, 1.4 deg^2, and 2.2 deg^2 fields of view, respectively. The main observations by the KMTNet and OGLE surveys were made in the I band, while MOA observations were made in the customized MOA-R band. For all surveys, a fraction of images were obtained in the V band for the color measurements of source stars. The data were reduced using the photometry pipelines of the individual survey groups: Albrow et al. (2009) for KMTNet, Udalski (2003) for OGLE, and Bond et al. (2001) for MOA. For each data set, the error bars from the photometry pipelines were readjusted to make the data consistent with the scatter of data and so that the χ^2 per degree of freedom becomes unity following the Yee et al. (2012) routine.

3. Procedures of event selection and modeling

We search for BDs belonging to binary lenses rather than single-mass BDs for two main reasons. First, the lensing parameter of the companion-to-primary mass ratio, q, can be securely measured for general binary-lens events, and thus it is possible to pick out BD candidates from the measured mass ratios. Considering that typical Galactic lensing events are produced by low-mass stars (Han & Gould 2003), companions of binary lenses with mass ratios $q \lesssim 10^{-1}$ are very likely to be BDs. Second, anomalies in binary-lens events often involve caustics, and thus it is possible to measure an additional observable of the angular Einstein radius $\theta_{\rm E}$, which is difficult to measure for general single-lens events; but see Gould et al. (2022) for a systematic study. While the event timescale, $t_{\rm E}$, which is the basic lensing parameter measurable for both single and binary lens events, is related to the three physical lens parameters of the mass, M, and distance to the lens, $D_{\rm L}$, and the relative lens-source proper motion, μ, the Einstein radius is related to the two parameters of M and $D_{\rm L}$. Therefore, the mass of the companion can be more tightly constrained with the additional measurement of $\theta_{\rm E}$.

The binary-lens (2L1S) modeling of each lensing event is conducted following the common procedure described below. In the modeling, we search for a set of lensing parameters (solution) describing the observed lensing light curve. Under the assumption of a rectilinear lens-source relative motion (standard model), a binary-lensing light curve is described by seven lensing parameters. The first three parameters $(t_0, u_0, t_{\rm E})$ depict the approach of the source to the lens, and the individual parameters denote the time of the closest lens-source approach, the separation at that time (impact parameter), and the event timescale, respectively. The impact parameter is scaled to $\theta_{\rm E}$. Three other parameters (s, q, α) describe the binarity of the lens, and they represent the projected separation (normalized to $\theta_{\rm E}$) and mass ratio of the lens components, and the angle between the relative lens-source motion and the axis connecting the lens components (source trajectory angle). The last parameter ρ (normalized source radius), which is defined as the ratio of the angular source radius θ_* to $\theta_{\rm E}$, is included in modeling because a binary-lensing light curve usually exhibits anomalies resulting from caustic crossings or approaches, during which the light curve is affected by finite-source effects (Bennett & Rhie 1996).

Caustics represent source positions at which lensing magnifications of a point source become infinity. Binary caustics exist in three types of topology, referred to as "close", "intermediate", and "wide" binaries (Erdl & Schneider 1993; Dominik 1999). In the regime of the wide binary ($s \gg 1$), two sets of caustics form near the individual lens components. In the close-binary regime ($s \ll 1$), three caustic sets exist, one of which lies near the primary, and the other two lie away from the binary axis on the opposite side of the lens companion. In the intermediate regime, multiple sets of caustics merge to form a single large caustic, which is often referred to as a "resonant" caustic. See Fig. 1 of Cassan (2008) for the caustic topologies in the three regimes of binary lenses.

In addition to the basic parameters, binary-lens modeling occasionally requires including additional parameters for the description of higher-order effects in lensing light curves. One such higher-order effect is caused by the deviation of the source motion from a rectilinear one induced by the orbital motion of Earth: the microlens-parallax effect (Gould 1992). Another higher-order effect is caused by the variation in lens position that is induced by the orbital motion of the binary lens: the lens-orbital effect (Albrow et al. 2000). Considering these higher-order effects in modeling requires including additional parameters, which are $(\pi_{{\rm E},N}, \pi_{{\rm E},E})$ for the microlens-parallax effect and $({\rm d}s/{\rm d}t, {\rm d}\alpha/{\rm d}t)$ for the lens-orbital effects. The parameters $(\pi_{{\rm E},N}, \pi_{{\rm E},E})$ denote the components of the microlens-parallax vector $\boldsymbol{\pi}_{\rm E}$ that are projected onto the sky along the north and east directions, respectively, and the parameters $({\rm d}s/{\rm d}t, {\rm d}\alpha/{\rm d}t)$ represent the change rates of the binary separation and source trajectory angle, respectively. We note that the two-parameter description of the lens orbital motion is a local approximation of a more complete Keplerian model. The microlens-parallax vector is related to the relative lens-source parallax $\pi_{\rm rel} = {\rm AU}(D_{\rm L}^{-1} - D_{\rm S}^{-1})$ and the relative lens-source proper motion $\boldsymbol{\mu}$ by $\boldsymbol{\pi}_{\rm E} = (\pi_{\rm rel}/\theta_{\rm E})(\boldsymbol{\mu}/\mu)$.

The binary-lens modeling is carried out in two steps. In the first step, we search for the binary parameters (s, q) using a grid approach, while the other parameters are found using a downhill approach. We use the Markov chain Monte Carlo (MCMC) algorithm for the downhill approach. This first-step procedure yields a $\Delta\chi^2$ map on the s–q parameters plane, and we identify local solutions on the map, including those resulting from various types of degeneracy, if they exist. In the second step, we polish the individual local solutions by letting all parameters vary, including s and q. We present multiple solutions if degeneracies among different solutions are severe. We also check higher-order effects for well-covered lensing events with long timescales. For some anomalous events without obvious caustic-crossing features, we additionally check whether the observed anomalies can be explained by a binary-source interpretation (Gaudi 1998). In the subsequent subsections, we present the analyses of the individual events.

3.1. OGLE-2016-BLG-0890

The source of the lensing event OGLE-2016-BLG-0890 lies toward the Galactic bulge field with the equatorial coordinates $({\rm RA, Dec})_{\rm J2000}$ = (17:30:25.69, −29:50:48.98), which correspond to the Galactic coordinates (l, b) = (−2.°540, 2.°308).

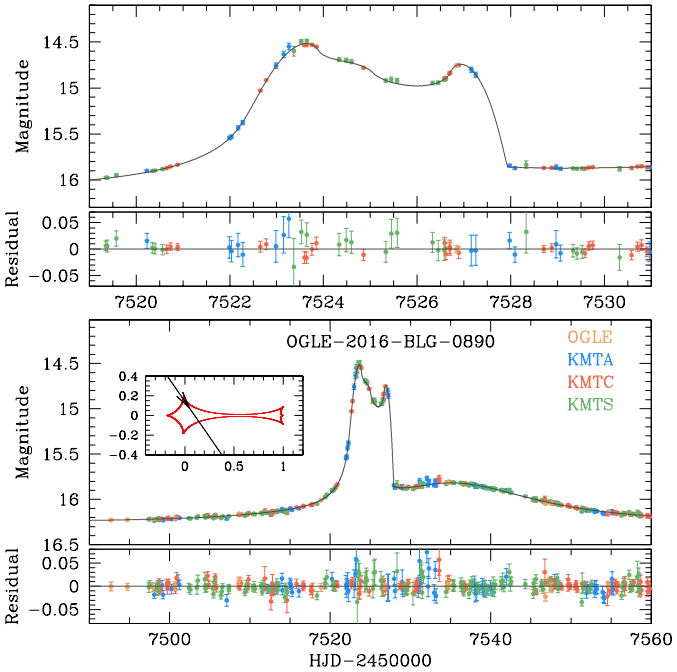

Fig. 1. Light curve and model of OGLE-2016-BLG-0890. Upper panel: enlargement of the major anomaly region and the residual from the model. The inset in the *lower panel* shows the lens-system configuration, in which the line with an arrow represents the source trajectory, and the red figure is the caustic.

Table 2. Model of OGLE-2016-BLG-0890.

Parameter	Value
χ^2/d.o.f.	723.97/717
t_0 (HJD′)	7525.298 ± 0.012
u_0	0.0817 ± 0.0010
t_E (days)	15.00 ± 0.06
s	1.594 ± 0.002
q	0.097 ± 0.002
α (rad)	4.103 ± 0.005
ρ (10^{-3})	40.79 ± 0.82

The baseline magnitude of the source is I_{base} = 16.25. The event was first found by the OGLE survey on 2016 May 18 (HJD′ ≡ HJD − 2 450 000 ∼ 7516), at which the source became brighter than the baseline by ∼0.16 mag. The event was also in the footprint of the KMTNet survey, and it was identified from the post-season investigation (Kim et al. 2018b) and designated as KMT-2016-BLG-0793.

The lensing light curve constructed from the combination of the OGLE and KMTNet data is presented in Fig. 1. It shows clear features of caustic crossings at HJD′ = 7522.35 and 7527.00, which correspond to the times of the caustic entrance and exit, respectively. Both caustic crossings were resolved by the data obtained from the combination of the KMTNet observations conducted with a cadence of 2.5 h. The light curve in the region between the two caustic-crossing features exhibits deviations from a typical U-shape pattern, and this suggests that the source passed along a fold of the caustic.

In Table 2 we list the lensing parameters found from the modeling. We found a unique solution with binary lensing parameters of $(s, q) \sim (1.59, 0.097)$. The inset in the lower panel of Fig. 1 shows the lens-system configuration, in which the source trajectory (line with an arrow) with respect to the caustic (closed red figure) is presented. For the coordinate center of the configuration, we adopted the barycenter for a close binary and the effective lens position, defined by Di Stefano & Mao (1996) and An & Han (2002), for a wide binary. In the case of OGLE-2016-BLG-0890, the coordinates are centered at the effective position of the lower-mass component, M_2, and thus the primary, M_1, is located on the right side. The topology of the binary lens corresponds to the intermediate regime forming a single merged resonant caustic. The normalized source radius, $\rho = (40.79 \pm 0.82) \times 10^{-3}$, of the lensing parameters is substantially larger than the typical value of about 10^{-3} for events involved with main-sequence source stars, and thus the source is likely to be a giant star. The source crossed the caustic lying around the lower-mass lens component with a source trajectory angle of $\alpha \sim 55°$. After the first caustic crossing, the source swept one fold of the caustic, and this caused the deviation of the light curve from a U-shape pattern in the region between the two caustic bumps. The weak bump at HJD′ ∼ 7535 was found to be produced by the source approach to the primary of the binary lens. The higher-order lensing parameters could not be securely constrained due to the short timescale of the event, $t_E \sim 15$ days.

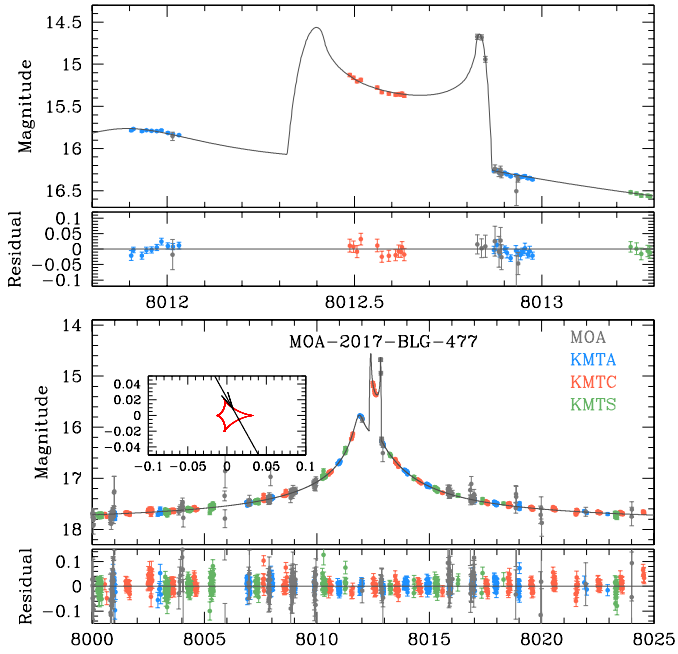

Fig. 2. Light curve and model of MOA-2017-BLG-477. Notations and arrangement of the panels are same as those in Fig. 1.

3.2. MOA-2017-BLG-477

The source of the lensing event MOA-2017-BLG-477, with a baseline magnitude of I_{base} = 18.02, lies at the equatorial coordinates $(RA, Dec)_{J2000}$ = (18 : 05 : 50.00, −27 : 04 : 38.50), which correspond to the Galactic coordinates (l, b) = (3°.854, −2°.918). The MOA group first found the event on 2017 September 15 (HJD′ ∼ 8011), which was one day before the event reached its peak. The event was also observed by the KMTNet group using its three telescopes, and it was designated as KMT-2017-BLG-1757.

Figure 2 shows the light curve constructed with the combined MOA and KMTNet data. The peak region of the light

Table 3. Models of MOA-2017-BLG-477.

Parameter	Close	Wide
χ^2/d.o.f.	9264.6/9249	9231.2/9249
t_0 (HJD′)	8012.543 ± 0.003	8012.527 ± 0.003
u_0	0.0109 ± 0.0002	0.0117 ± 0.0002
t_E (days)	25.10 ± 0.37	26.87 ± 0.36
s	0.355 ± 0.006	3.204 ± 0.066
q	0.097 ± 0.005	0.115 ± 0.007
α (rad)	4.224 ± 0.007	4.206 ± 0.006
ρ (10^{-3})	0.88 ± 0.06	0.80 ± 0.06

curve exhibits three bumps at $t_1 \sim 8012.0$, $t_2 \sim 8012.5$, and $t_3 \sim 8012.8$. The last peak, covered by the MOA data, appears to be a caustic-crossing bump from its shape. Considering that caustic bumps appear in pairs, the bump at t_2 would correspond to the U-shape region between a pair of caustic bumps arising after an uncovered bump generated by the source star's caustic entrance. The light-curve profile of the bump at t_1 is rather smooth, suggesting that this bump would be produced by a source approach to a cusp of a caustic.

We found two sets of solutions in our modeling, one in the close-binary regime and the other in the wide-binary regime. The two solutions result from the well-known close–wide degeneracy, which was first mentioned by Griest & Safizadeh (1998), and later its origin was investigated by Dominik (1999) and An (2005). The binary lensing parameters are $(s, q)_{\rm close} \sim (0.36, 0.10)$ for the close solution and $(s, q)_{\rm wide} \sim (3.20, 0.11)$ for the wide solution. The full lensing parameters of the individual solutions are presented in Table 3. The wide solution yields a better fit to the data than the close solution by $\Delta\chi^2 = 33.4$, which corresponds to a difference of $\sqrt{\Delta\chi^2} = 5.8\sigma$ assuming a Gaussian error distribution.

The lens-system configuration corresponding to the wide solution is shown in the inset of the lower panel in Fig. 2. Because the lens is in the wide-binary regime, there are two sets of caustics according to this solution, and we present the region around the caustic through which the source passed. As expected, the bump at t_3 was produced by the caustic exit of the source, and the bump at t_1 was generated by the cusp approach of the source. According to the model, the source entered the caustic at HJD′ ∼ 8012.42, which could have been covered by the KMTS data if the sky had not been clouded out. Fortunately, the caustic exit was resolved by the three data points acquired from MOA observations, and this enables us to measure the normalized source radius of $\rho \sim 0.8 \times 10^{-3}$. The event timescale, $t_E \sim 27$ days, is not long enough for us to securely measure the higher-order lensing parameters.

3.3. OGLE-2017-BLG-0614

The source star of the event OGLE-2017-BLG-0614, lying at the equatorial coordinates of $(\mathrm{RA}, \mathrm{Dec})_{\rm J2000} = (17{:}26{:}08.08, -30{:}17{:}46.14)$ and Galactic coordinates of $(l, b) = (-3.^\circ430, 2.^\circ833)$, is very faint, with a baseline magnitude of $I_{\rm base} = 20.04$. The alert of the event was issued on 2017 April 23 (HJD′ ∼ 7867.4) by the OGLE group at around the peak time of the light curve. There appeared to be a single anomalous point around the peak at HJD′ ∼ 7863 in the OGLE data, but it was difficult to determine its nature due to the lack of data covering the anomaly. The KMTNet group also found the event, labeled KMT-2017-BLG-2209, from the postseason analysis, and found that the peak region was well covered by the data from the three KMTNet telescopes.

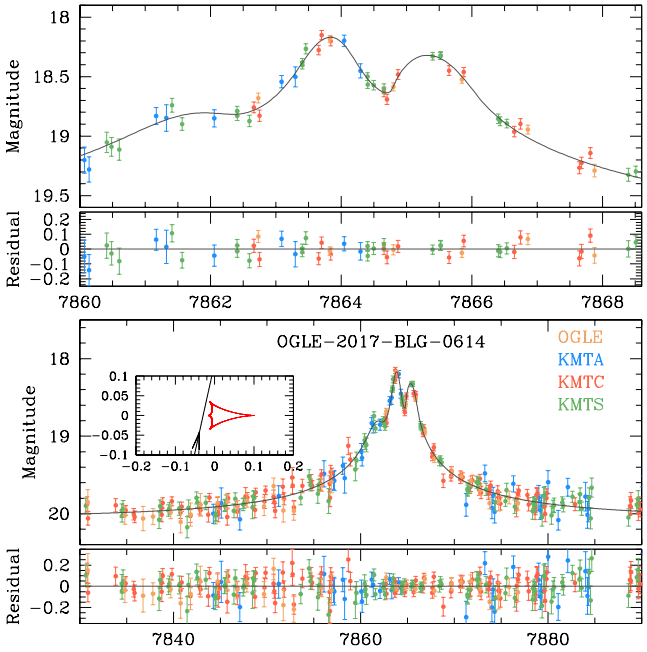

Fig. 3. Light curve and model of OGLE-2017-BLG-0614.

Table 4. Models of OGLE-2017-BLG-0614.

Parameter	Close	Wide
χ^2/d.o.f.	732.1/724	730.4/724
t_0 (HJD′)	7863.991 ± 0.022	7863.991 ± 0.023
u_0	0.028 ± 0.004	0.029 ± 0.003
t_E (days)	40.64 ± 4.70	39.82 ± 4.09
s	0.533 ± 0.016	1.842 ± 0.073
q	0.049 ± 0.006	0.050 ± 0.006
α (rad)	1.802 ± 0.020	1.788 ± 0.021
ρ (10^{-3})	–	–

The light curve of OGLE-2017-BLG-0614 constructed by combining the OGLE and KMTNet data sets is displayed in Fig. 3. It shows three smooth bumps around the peak region: a weak bump at $t_1 \sim 7861.3$, and two relatively strong bumps at $t_2 \sim 7863.5$ and $t_3 \sim 7865.3$. The single anomalous OGLE data point corresponds to the peak of the second bump. In general, a caustic crossing produces a sharp spike feature, but the feature can be smooth if the source is substantially larger than the caustic. For OGLE-2017-BLG-0614, however, the source is likely to be a very faint star, meaning that the source is unlikely to be large enough to make caustic-crossing features smooth. This implies that all the three observed bumps are likely to be produced by the successive approaches of the source to three cusps of a caustic.

Modeling the light curve yielded two sets of solutions resulting from the close–wide degeneracy, with binary parameters of $(s, q)_{\rm close} \sim (0.53, 0.05)$ and $(s, q)_{\rm wide} \sim (1.84, 0.05)$ for the close and wide solutions, respectively. The full lensing parameters of the two solutions are listed in Table 4. The degeneracy between the two solutions is severe, and the wide model is preferred only by $\Delta\chi^2 = 1.7$. The lens system configuration for the wide solution is presented in the inset of the lower panel of Fig. 3. We

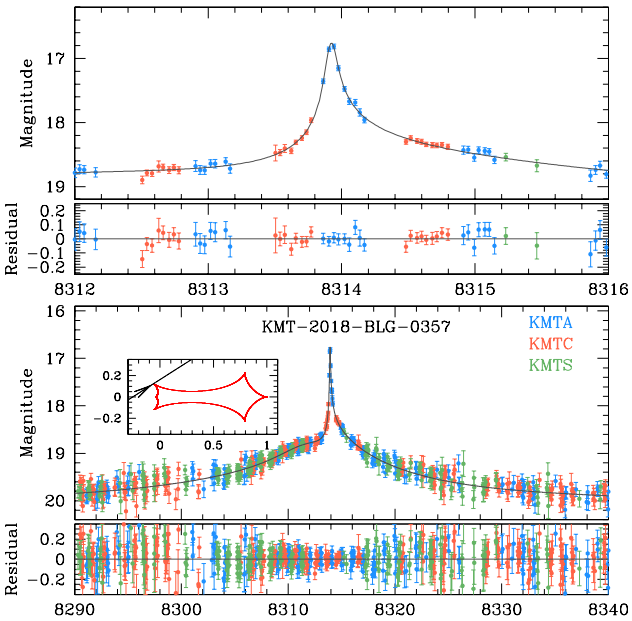

Fig. 4. Light curve and model of KMT-2018-BLG-0357.

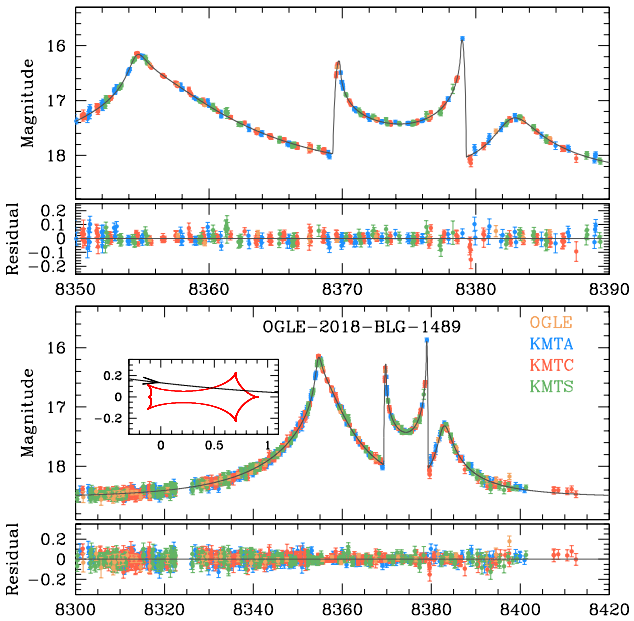

Fig. 5. Light curve and model of OGLE-2018-BLG-1489.

Table 5. Models of KMT-2018-BLG-0357.

Parameter	Close	Wide
χ^2/d.o.f.	1510.5/1483	1490.6/1483
t_0 (HJD′)	8313.012 ± 0.079	8313.476 ± 0.069
u_0	0.131 ± 0.0159	0.138 ± 0.013
t_E (days)	28.25 ± 2.27	26.70 ± 2.19
s	0.672 ± 0.012	1.461 ± 0.033
q	0.094 ± 0.009	0.111 ± 0.009
α (rad)	2.472 ± 0.027	2.574 ± 0.028
ρ (10^{-3})	1.57 ± 0.49	1.27 ± 0.46

note that the configuration of the close solution is similar to it. According to the configuration, the bumps were produced by the successive approaches of the source to the three cusps of the caustic, as expected from the shapes of the bumps. These successive approaches were possible because the three cusps of the caustic lie on one side of the primary star due to the low mass ratio, $q \sim 0.05$, of the lens components. The strength of the bump varies depending on the combination of the strength of the cusp and the separation from the source. Because none of the bumps was produced by a caustic crossing, the normalized source radius could not be measured. Furthermore, the higher-order lensing parameters were difficult to measure because the precision of the photometric data is not high enough to detect the subtle deviations induced by the higher-order effects.

3.4. KMT-2018-BLG-0357

The lensing event KMT-2018-BLG-0357 was observed solely by the KMTNet survey. The alert on the detection of the event was issued on 2018 July 30 (HJD′ ∼ 8330) with the operation of the AlertFinder system of the KMTNet survey. The source, lying at (RA, DEC)$_{J2000}$ = (17:44:12.20, −33:36:23.18) and (l, b) = (−4°.143, 2°.180), has a baseline magnitude of I_{base} = 19.92.

Figure 4 shows the light curve of the event constructed with the use of the three data sets from the KMTA, KMTC, and KMTS telescopes. It exhibits a strong short-term anomaly near the peak at around HJD′ ∼ 8313.8. The central part of the anomaly was covered by the KMTA data set, and the peripheral parts on the rising and falling sides were covered by the KMTC data set. The anomaly exhibits a typical pattern arising when a source approaches or crosses the tip of a caustic cusp.

According to the models, the anomaly was produced by a binary containing a low-mass companion. We find two solutions with $(s, q)_{close} \sim (0.67, 0.09)$ and $(s, q)_{wide} \sim (1.46, 0.11)$, between which the wide solution is preferred over the close solution by $\Delta\chi^2 = 19.9$. The full lensing parameters of the two solutions are listed in Table 5.

Considering that a short-term anomaly can be produced by a binary companion to the source (Gaudi 1998), we additionally conducted a binary-source modeling. This modeling excludes the binary-source interpretation of the anomaly with a strong statistical confidence of $\Delta\chi^2 = 480$.

In the inset of the lower panel in Fig. 4, we present the lens-system configuration corresponding to the wide solution. It shows that the binary lens is in the intermediate regime with a single merged caustic, and the anomaly was produced by the source crossing over the tip of the off-axis cusp that is closer to the heavier lens component. The caustic crossing allows us to measure the normalized source radius of $\rho \sim 1.3\times10^{-3}$, although its uncertainty is fairly large.

3.5. OGLE-2018-BLG-1489

The lensing magnification of the event OGLE-2018-BLG-1489 occurred on a source lying at (RA, Dec)$_{J2000}$ = (17:45:46.60, −23:57:43.85), which corresponds to (l, b) = (4°.267, 2°.559). The baseline magnitude of the source was I_{base} = 18.55. The event was first found by the OGLE group on 2018 August 12 (HJD′ ∼ 8343.4) when the source flux was magnified by about 2.5 mag. The event was found independently by the KMTNet group, who labeled the event KMT-2018-BLG-1534, from the postseason investigation of the data obtained during the 2018 season.

The light curve, shown in Fig. 5, exhibits a complex pattern with four peaks: at HJD′ ∼ 8354.1 (t_1), 8369.7 (t_2), 8378.7 (t_3),

Table 6. Models of OGLE-2018-BLG-1489.

Parameter	Standard	Higher order
χ^2/d.o.f.	2094.2/2111	2039.6/2108
t_0 (HJD′)	8357.396 ± 0.014	8359.221 ± 0.047
u_0	0.139 ± 0.001	0.132 ± 0.001
$t_{\rm E}$ (days)	25.99 ± 0.04	26.48 ± 0.17
s	1.414 ± 0.001	1.436 ± 0.006
q	0.097 ± 0.001	0.103 ± 0.002
α (rad)	3.262 ± 0.002	3.257 ± 0.004
ρ (10^{-3})	3.93 ± 0.14	3.86 ± 0.17
$\pi_{{\rm E},N}$	–	−0.059 ± 0.51
$\pi_{{\rm E},E}$	–	−0.023 ± 0.06
ds/dt (yr^{-1})	–	−0.72 ± 0.16
$d\alpha/dt$ (rad yr^{-1})	–	0.07 ± 0.69

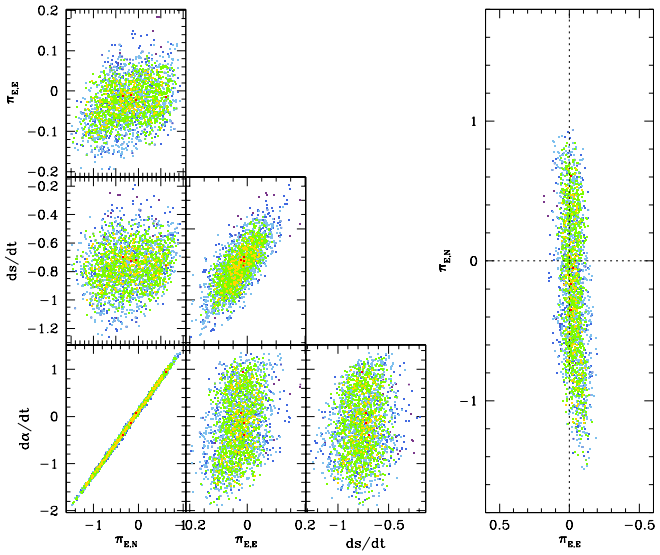

Fig. 6. Scatter plot of points in the MCMC chain on the planes of higher-order lensing parameters of the lensing event OGLE-2018-BLG-1489. The plot on the $\pi_{{\rm E},E}$–$\pi_{{\rm E},N}$ parameter plane is separately presented in the *right panel*. The colors are set to indicate points with ≤1σ (red), ≤2σ (yellow), ≤ 3σ (green), ≤ 4σ (cyan), and ≤ 5σ (blue).

and 8382.5 (t_4). All the anomaly features were well delineated by the data from the KMTNet observations conducted with a one-hour cadence using its three telescopes. From the sharp rise and fall of the light curve, it appears that the two peaks at t_2 and t_3 were produced by the caustic crossings of the source. On the other hand, from the smooth rising and declining of the light curve, it appears that the two peaks at t_1 and t_4 were produced by the cusp approaches. The rising part of the caustic entrance at t_2 was partially resolved by the KMTC data, thus allowing the normalized source radius to be measured.

A 2L1S modeling of the light curve yielded a unique solution with binary parameters of $(s, q) \sim (1.41, 0.1)$. We list the full lensing parameters in Table 6. In the inset of the lower panel in Fig. 5, we present the configuration of the lens system. It shows that the caustic is in the resonant regime, in which a single merged caustic is elongated along the binary axis. The source closely approached the upper left cusp at t_1, entered the caustic at t_2, exited the caustic at t_3, and then passed by the right on-axis cusp of the caustic. The measured value of the normalized source radius is $\rho = (3.93 \pm 0.14) \times 10^{-3}$.

Because the event was continuously covered with a relative good photometric precision, we checked whether the higher-order lensing parameters could be constrained. From an additional modeling, it was found that considering the higher-order effects substantially improved the model fit by $\Delta\chi^2 = 54.6$. The lensing parameters obtained from this modeling are listed in Table 6. However, the uncertainties of the measured microlens-parallax parameters are large. In Fig. 6 we present the scatter plots of MCMC points on the planes of higher-order parameters. The $\pi_{{\rm E},E}$–$\pi_{{\rm E},N}$ plot, which is separately presented on the right side, shows that the uncertainty of the north component of the parallax vector is substantial. In the higher-order modeling, we imposed the restriction that the projected kinetic-to-potential energy ratio is lower than $({\rm KE/PE})_\perp \le 0.8$. The ratio is computed from the lensing parameters by

$$\left(\frac{\rm KE}{\rm PE}\right)_\perp = \frac{(a_\perp/{\rm AU})}{8\pi^2(M/M_\odot)}\left[\left(\frac{1}{s}\frac{ds}{dt}\right)^2 + \left(\frac{d\alpha}{dt}\right)^2\right]. \quad (1)$$

Here $a_\perp = D_{\rm L}\theta_{\rm E}$ is the projected semi-major axis, M and $D_{\rm L}$ denote the mass and distance to the lens, respectively, which are related to the lensing parameters by

$$M = \frac{\theta_{\rm E}}{\kappa\pi_{\rm E}}; \qquad D_{\rm L} = \frac{\rm AU}{\pi_{\rm E}\theta_{\rm E} + \pi_{\rm S}}, \quad (2)$$

where $\pi_{\rm E} = (\pi_{{\rm E},N}^2 + \pi_{{\rm E},E}^2)^{1/2}$, $\kappa = 4G/(c^2{\rm AU})$, and $\pi_{\rm S} = {\rm AU}/D_{\rm S}$ (Gould 2000). It is known that there exists a degeneracy between the parallax and orbital effects, as discussed in detail by Skowron et al. (2011). From the combined facts that the region around $(\pi_{{\rm E},E}, \pi_{{\rm E},N}) = (0, 0)$ is within 2σ region from the best-fit model and that the orbital parameter $|ds/dt| \sim 0.8$, the improvement of the fit relative to the standard model is mostly ascribed to the lens-orbital effect rather than the microlens-parallax effect. Nevertheless, one component of the microlens parallax, that is, $\pi_{{\rm E},E}$, is well constrained.

3.6. OGLE-2018-BLG-0360

The source star of the lensing event OGLE-2018-BLG-0360 lies at the equatorial and Galactic coordinates of $({\rm RA, Dec})_{\rm J2000} = (17:52:01.26, -31:08:54.71)$ and $(l, b) = (1^\circ.183, -2^\circ.326)$, respectively. The baseline magnitude of the source is $I_{\rm base} = 19.28$. The event was observed by all of the three currently operating microlensing surveys. The OGLE group first detected the event on 2018 March 15 (HJD′ = 8193.4), the MOA group, who labeled the event MOA-2018-BLG-116, found it on 2018-04-22 (HJD′ = 8231.4), and the KMTNet group identified the event, labeled KMT-2018-BLG-2014, from the postseason investigation of the data.

Figure 7 shows the light curve of the event constructed by combining the data from the three survey experiments. It shows the characteristic pattern of a binary-lens event with two caustic-crossing spikes, for which the first spike at HJD′ ∼ 8230 was covered by the combination of MOA, KMTA, and KMTS data sets, and the second one at HJD′ ∼ 8242 was resolved by the MOA data set. In addition to these spikes, there is a weak bump at HJD′ ∼ 8228.

Modeling the light curve yielded a unique solution with binary parameters of $(s, q) \sim (1.06, 0.06)$, indicating that the event was produced by a binary in an intermediate regime with a low-mass companion. We list the full lensing parameters in Table 7. The normalized source radius estimated from the analysis of the caustic-crossing parts is $\rho = (2.18 \pm 0.04) \times 10^{-3}$.

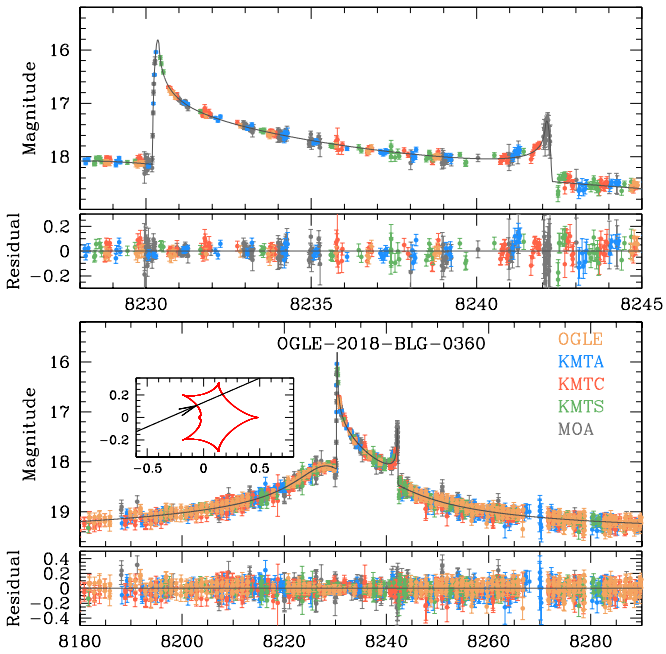

Fig. 7. Light curve and model of OGLE-2018-BLG-0360.

Table 7. Model of OGLE-2018-BLG-0360.

Parameter	Value
χ^2/d.o.f.	3576.3/3569
t_0 (HJD′)	8230.867 ± 0.048
u_0	0.122 ± 0.002
$t_{\rm E}$ (days)	47.63 ± 0.78
s	1.056 ± 0.003
q	0.063 ± 0.002
α (rad)	2.732 ± 0.010
ρ (10^{-3})	2.18 ± 0.04

According to the lens-system configuration, presented in the inset of the lower panel, the spikes were produced by the source crossings over the two folds of the six-sided resonant caustic that are separated by consecutive off-axis cusps, and the weak bump was produced by the approach of the source close to the on-axis cusp near the host. From the modeling considering higher-order effects, it was found that the microlens parallax was difficult to measure securely because of the moderate photometric precision of the data.

4. Source stars and angular Einstein radii

For five out of the six analyzed lensing events, the normalized source radii were securely measured from the deviations of the light curves affected by finite-source effects. In this section, we estimate the angular Einstein radii for these events. The value of $\theta_{\rm E}$ is estimated from the measured ρ value by

$$\theta_{\rm E} = \frac{\theta_*}{\rho}, \quad (3)$$

where the angular source radius θ_* is estimated from the color and brightness of the source. Although the Einstein radius cannot be measured for OGLE-2017-BLG-0614 because the ρ value could not measured, we estimate θ_* for the full characterization of the event.

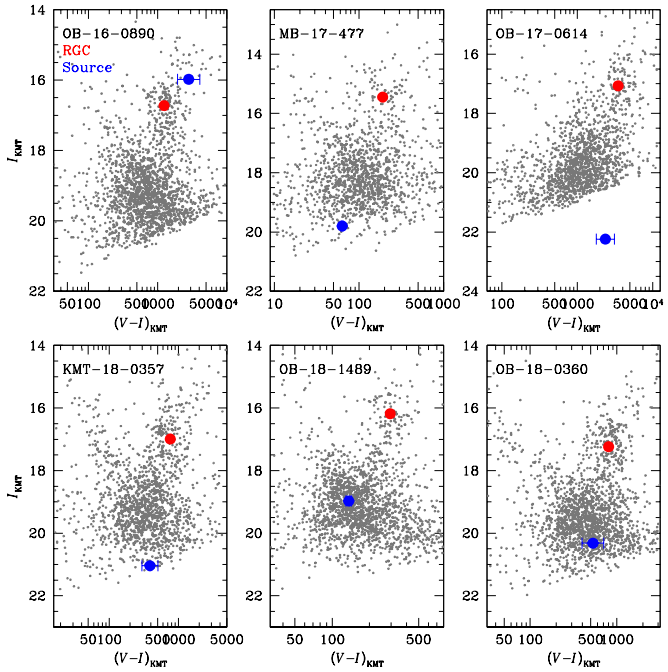

Fig. 8. Locations of the source stars (filled blue dots) of the individual events with respect to the centroids of the red giant clump (red dot) in the instrumental CMDs constructed from the pyDIA photometry of KMTNet data.

The angular source radius of each event was estimated from the $V-I$ color and I-band magnitude. To estimate the reddening and extinction-corrected (dereddened) color and magnitude, $(V-I, I)_{0,\rm S}$, from instrumental values, we applied the method of Yoo et al. (2004). In this method, the centroid of the red giant clump (RGC), with known dereddened values of $(V-I, I)_{0,\rm RGC}$, in the color-magnitude diagram (CMD) is used as a reference to convert instrumental color and magnitude $(V-I, I)$ into $(V-I, I)_{0,\rm S}$, that is,

$$(V-I, I)_{0,\rm S} = (V-I, I)_{0,\rm RGC} + [(V-I, I)_{\rm S} - (V-I, I)_{\rm RGC}]. \quad (4)$$

Here $(V-I, I)_{\rm S}$ and $(V-I, I)_{\rm RGC}$ denote the instrumental colors and magnitudes of the source and RGC, respectively, and thus the term in the brackets on the right side of Eq. (4) indicates the offsets in color and magnitude of the source from the RGC centroid in the instrumental CMD. For this conversion, the dereddened color, $(V-I)_{0,\rm RGC} = 1.06$, and magnitude of the RGC centroid were adopted from Bensby et al. (2013) and Nataf et al. (2013), respectively.

Figure 8 shows the instrumental CMDs of stars lying near the source stars of the individual events constructed with the use of the photometry data processed using the pyDIA (Albrow 2017) reductions of the KMTC data. In each diagram, we mark the locations of the source and RGC, indicated by filled red and blue dots, respectively. The I- and V-band magnitudes of each source were measured from the regression of the photometry data in the individual passbands processed using the same pyDIA code with the variation of the lensing magnification. In Table 8 we summarize the values of $(V-I, I)_{\rm S}$, $(V-I, I)_{\rm RGC}$, $I_{\rm RGC}$, and $(V-I, I)_{0,\rm S}$ for the individual events. According to the estimated values of $(V-I, I)_{0,\rm S}$, it is found that the source of OGLE-2016-BLG-0890 is a K-type giant, and those of the other events are main-sequence stars with spectral types ranging from G to K. We then converted $V-I$ into $V-K$ using the color-color relations of Bessell & Brett (1988) and then derived θ_* from the

Table 8. Properties of source stars.

Events	$(V-I, I)_S$	$(V-I, I)_{RGC}$	$I_{0,RGC}$	$(V-I, I)_{0,S}$	θ_* (μas)
OGLE-2016-BLG-0890	(3.45 ± 0.16, 15.979 ± 0.001)	(3.09, 16.725)	14.573	(1.42 ± 0.16, 13.827 ± 0.001)	10.35 ± 1.82
MOA-2017-BLG-477	(1.80 ± 0.01, 19.800 ± 0.005)	(2.28, 15.448)	14.332	(0.58 ± 0.10, 18.684 ± 0.005)	0.50 ± 0.04
OGLE-2017-BLG-0614	(3.37 ± 0.12, 22.242 ± 0.005)	(3.54, 17.067)	14.596	(0.89 ± 0.12, 19.771 ± 0.005)	0.43 ± 0.06
KMT-2018-BLG-0357	(2.59 ± 0.12, 21.040 ± 0.011)	(2.88, 16.993)	14.372	(0.77 ± 0.12, 18.423 ± 0.011)	0.69 ± 0.09
OGLE-2018-BLG-1489	(2.14 ± 0.02, 18.970 ± 0.003)	(2.47, 16.182)	14.322	(0.73 ± 0.02, 17.110 ± 1.003)	1.36 ± 0.10
OGLE-2018-BLG-0360	(2.73 ± 9.13, 20.319 ± 0.008)	(2.91, 17.238)	14.512	(0.88 ± 0.13, 17.593 ± 0.008)	1.15 ± 0.30

Notes. $(V-I)_{0,RGC} = 1.06$.

Table 9. Einstein radius and proper motion.

Event	θ_E (mas)	μ (mas yr^{-1})
OGLE-2016-BLG-0890	0.26 ± 0.05	6.30 ± 1.12
MOA-2017-BLG-477	0.67 ± 0.06	9.33 ± 0.83
OGLE-2017-BLG-0614	–	–
KMT-2018-BLG-0357	0.57 ± 0.08	7.52 ± 1.05
OGLE-2018-BLG-1489	0.36 ± 0.03	4.89 ± 0.36
OGLE-2018-BLG-0360	0.53 ± 0.08	4.12 ± 0.59

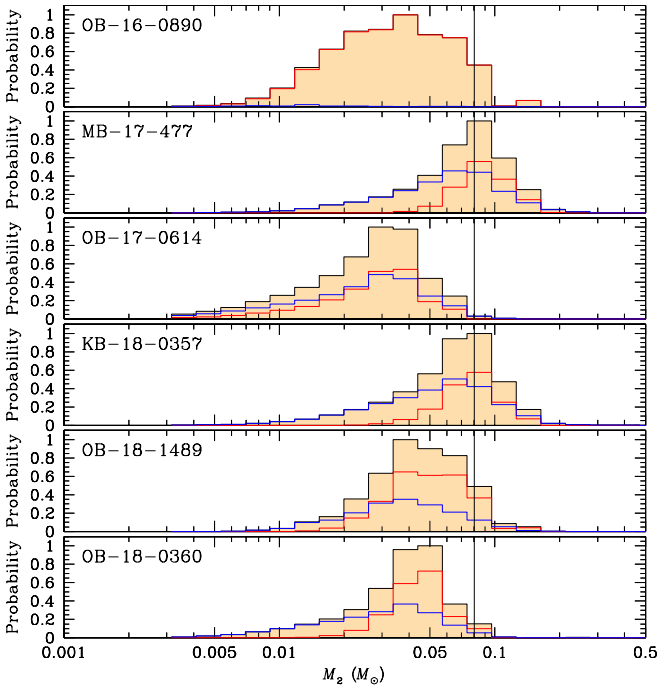

Fig. 9. Bayesian posterior for the companion masses of the binary lenses. The solid vertical line in each panel represents the mass boundary between a BD and a star. The blue and red curves represent the contributions by the disk and bulge lens populations, respectively, and the black curve is the sum of the contributions.

Kervella et al. (2004) relation between $(V-K, V)$ and θ_*. The estimated source radii of the individual events are listed in the last column of Table 8.

With the measured source radii, the angular Einstein radii of the events were estimated using the relation in Eq. (3). With the measured event timescale, the relative proper motion between

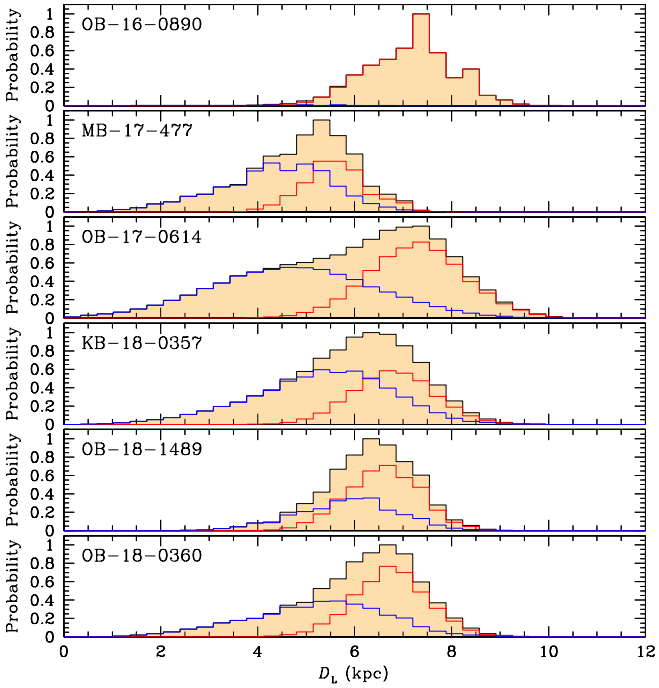

Fig. 10. Bayesian posterior for the distances to the lens systems. The notations are same as those in Fig. 9.

the lens and source was estimated by

$$\mu = \frac{\theta_E}{t_E}. \quad (5)$$

In Table 9 we list the estimated values of θ_E and μ of the individual events. In the cases of the events MOA-2017-BLG-477 and KMT-2018-BLG-0357, for which two models were presented, we present θ_E and μ values estimated from the wide models, which yield better fits over the corresponding close solutions with significant confidence levels of $\Delta\chi^2 = 33.4$ and 19.9, respectively. It was found that the Einstein radii of the events lie in the range of [0.26–0.67] mas, and the proper motions are in the range of [4.1–9.3] mas yr^{-1}.

5. Physical lens properties

In addition to the basic observable of t_E, unique determinations of the lens mass and distance require the two additional observables of θ_E and π_E to be measured by the relation given in Eq. (2). For all events except OGLE-2018-BLG-1489, the microlens-parallax could not be measured, and even for OGLE-2018-BLG-1489, the uncertainty of the measured π_E is very large, as shown

Table 10. Physical lens parameters.

Events	M_1 ($M_\odot$)	M_2 ($M_\odot$)	D_L (kpc)	$a_\perp$ (AU)	P_{BD} (%)	P_{star} (%)	P_{planet} (%)	P_{disk} (%)	P_{bulge} (%)
OGLE-2016-BLG-0890	$0.40^{+0.35}_{-0.20}$	$0.038^{+0.033}_{-0.020}$	$7.4^{+0.8}_{-1.1}$	$3.5^{+0.4}_{-0.4}$	86	5	9	1	99
MOA-2017-BLG-477 (wide)	$0.74^{+0.33}_{-0.36}$	$0.085^{+0.040}_{-0.041}$	$5.0^{+1.0}_{-1.4}$	$10.5^{+2.0}_{-3.0}$	61	37	2	62	38
OGLE-2017-BLG-0614 (close)	$0.64^{+0.38}_{-0.37}$	$0.031^{+0.019}_{-0.018}$	$6.4^{+1.6}_{-2.4}$	$1.8^{+0.4}_{-0.7}$	81	1	18	53	47
(wide)	–	$0.032^{+0.019}_{-0.018}$	–	$6.0^{+1.5}_{-2.3}$	–	–	–	–	
KMT-2018-BLG-0357 (wide)	$0.68^{+0.34}_{-0.34}$	$0.075^{+0.035}_{-0.036}$	$6.2^{+1.2}_{-1.7}$	$5.0^{+1.0}_{-1.3}$	69	28	3	62	38
OGLE-2018-BLG-1489	$0.48^{+0.32}_{-0.19}$	$0.050^{+0.031}_{-0.020}$	$6.5^{+0.9}_{-1.0}$	$3.5^{+0.5}_{-0.5}$	89	9	2	39	61
OGLE-2018-BLG-0360	$0.72^{+0.31}_{-0.35}$	$0.045^{+0.019}_{-0.021}$	$6.4^{+0.1}_{-1.6}$	$3.6^{+0.6}_{-0.9}$	90	2	8	49	51

in Fig. 6. As a result, it is difficult to uniquely determine M and D_L from the relations in Eq. (2). Although the π_E constraint is either unavailable or weak, the physical lens parameters can still be constrained using the other observables with the use of a Galactic model that defines the distributions of the mass density, motion, and mass function of Galactic objects. For these constraints, we conducted Bayesian analyses of the individual events.

The Bayesian analyses were conducted according to the following procedure. In the first step, we generated a large number (6×10^6) of artificial lensing events. For the individual events, their physical parameters of the lens mass M, distances to the lens D_L and source D_S, and lens-source transverse velocity $v_\perp$ were assigned from the Monte Carlo simulation conducted with the use of a Galactic model. In the simulation, we adopted the Jung et al. (2021) Galactic model. For the mass density distribution, the Galactic model uses the Robin et al. (2003) disk model and the Han & Gould (2003) bulge model. For the kinematic distribution of disk objects, the model uses the modified version of the Han & Gould (1995) model, in which the original version based on the double-exponential disk model was modified to reconcile it with the Robin et al. (2003) density distribution. For the kinematic distribution of bulge objects, the model was constructed based on the proper motions of stars in the *Gaia* catalog (Gaia Collaboration 2016, 2018). For the mass functions of bulge and disk populations, the Galactic model adopted the initial mass function and the present-day mass function of Chabrier (2003), respectively. See Jung et al. (2021) for details of the Galactic model.

In the second step, we constructed the posterior distributions of the physical lens parameters. For this, we first computed event timescales and Einstein radii of the artificial events produced by the simulation as $t_{E,i} = D_L\theta_{E,i}/v_\perp$ and $\theta_{E,i} = (\kappa M\pi_{rel})^{1/2}$, respectively. Then, the Bayesian posteriors of each lensing event were constructed by assigning a weight for each artificial event as $w_i = \exp(-\chi^2/2)$. Here $\chi^2 = (t_{E,i}-t_E)^2/[\sigma(t_E)]^2 + (\theta_{E,i}-\theta_E)^2/[\sigma(\theta_E)]^2$, where $[t_E, \sigma(t_E)]$ and $[\theta_E, \sigma(\theta_E)]$ are the measured values of t_E and θ_E and their uncertainties, respectively. We note that only t_E is measured for OGLE-2017-BLG-0614, while both observables of t_E and θ_E are measured for the other events. In the case of OGLE-2018-BLG-1489, for which the model with higher-order effects is better than the standard model with $\Delta\chi^2 = 54.6$, we imposed an additional constraint of $\boldsymbol{\pi}_E$ given by the covariance matrix of the parallax ellipse presented in Fig. 6. In the cases of the events MOA-2017-BLG-477 and KMT-2018-BLG-0357, for which the wide solutions are favored over the close solutions with significant statistical confidence, we conducted Bayesian analyses for the wide solutions. In the case of OGLE-2017-0614, for which the degeneracy is very severe, we carried out a Bayesian analysis for both the close and wide solutions. The source star of OGLE-2016-BLG-0890 is bright, and thus it is registered in the *Gaia* catalog. In this case, we used the additional constraint of the source proper motion, $(\mu_E, \mu_N) = (-5.170 \pm 0.180, -11.385 \pm 0.123)$ mas yr^{-1}, in the Bayesian analysis.

Figures 9 and 10 show the posterior distributions of the companion lens mass and the distance to the lens systems for the individual lensing events, respectively. For each distribution, the blue and red curves represent the contributions by the disk and bulge lens populations, respectively, and the black curve is sum of the contributions from the two lens populations. In Table 10 we summarize the values of M_1, M_2, D_L, and $a_\perp$, for which the median values are listed as representative values, the uncertainties are estimated as the 16% and 84% of the posterior distributions, and $a_\perp = sD_L\theta_E$ represents the projected separation between the binary lens components. The table also lists the probabilities for the individual events that the lens companions are BD (P_{BD}), star (P_{star}), or planet (P_{planet}) and disk (P_{disk}) or bulge (P_{bulge}) members. According to the posteriors of M_2, the probabilities for the lens companions of the events OGLE-2016-BLG-0890, OGLE-2017-BLG-0614, OGLE-2018-BLG-1489, and OGLE-2018-BLG-0360 to be in the BD mass regime of [0.012 – 0.08] $M_\odot$ are very high with $P_{BD} > 80\%$. For MOA-2017-BLG-477 and KMT-2018-BLG-0357, the probabilities are $P_{BD} = 61\%$ and 69%, respectively, and the possibility that the companions of the lenses are very low-mass stars cannot be completely ruled out. In our Bayesian analyses, we assumed that the primary and companion follow the same mass function. If the number of companions in the BD regime declines compared to the mass function of the primary, that is, in the BD desert, for example (Grether & Lineweaver 2006), the BD probability P_{BD} would be lower than the presented probabilities.

6. Summary and conclusion

We investigated the microlensing survey data collected during the 2016–2018 seasons with the aim of finding microlensing binaries containing BD companions. In order to sort out BD-companion binary-lens events, we modeled all lensing events that were detected during the seasons with lensing light curves exhibiting anomaly features that were likely to be produced by binary lenses, and then applied the criterion that the companion-to-primary mass ratio was lower than 0.1. With this procedure, we found six candidate BD binary events: OGLE-2016-BLG-0890, MOA-2017-BLG-477, OGLE-2017-BLG-0614, KMT-2018-BLG-0357, OGLE-2018-BLG-1489, and OGLE-2018-BLG-0360, for which analyses had not been presented before.

For the identified candidate events, we conducted detailed modeling using optimized photometry data and checked possible degenerate interpretations caused by various types of degeneracies. We also checked the feasibility of detecting higher-order effects. We presented the solutions of the individual events and the corresponding lens-system configurations.

According to the estimated masses of the binary companions, we found that the probabilities that the lens companions of the events OGLE-2016-BLG-0890, OGLE-2017-BLG-0614, OGLE-2018-BLG-1489, and OGLE-2018-BLG-0360 are in the BD mass regime were very high. For the companions of the events MOA-2017-BLG-477 and KMT-2018-BLG-0357, it was found that the median masses were near the star-BD boundary, and thus the possibilities that the companions of the lenses were very low-mass stars could not be completely ruled out.

Acknowledgements. Work by C.H. was supported by the grants of National Research Foundation of Korea (2020R1A4A2002885 and 2019R1A2C2085965). This research has made use of the KMTNet system operated by the Korea Astronomy and Space Science Institute (KASI) and the data were obtained at three host sites of CTIO in Chile, SAAO in South Africa, and SSO in Australia. The MOA project is supported by JSPS KAKENHI Grant Number JSPS24253004, JSPS26247023, JSPS23340064, JSPS15H00781, JP16H06287, and JP17H02871. J.C.Y. acknowledges support from NSF Grant No. AST-2108414. W.Z. and H.Y. acknowledge support by the National Science Foundation of China (Grant No. 12133005). C.R. was supported by the Research fellowship of the Alexander von Humboldt Foundation.

References

Albrow, M., Horne, K., Bramich, D. M., et al. 2009, MNRAS, 397, 2099
Albrow, M. 2017, https://doi.org/10.5281/zenodo.268049
Albrow, M. D., Beaulieu, J.-P., Caldwell, J. A. R., et al. 2000, ApJ, 534, 894
Alcock, C., Allsman, R. A., Axelrod, T. S., et al. 1996, ApJ, 461, 84
An, J. H. 2005, MNRAS, 356, 1409
An, J. H., & Han, C. 2002, ApJ, 573, 351
Aubourg, E., Bareyre, P., Brehin, S., et al. 1995, A&A, 301, 1
Bennett, D. P., & Rhie, S. H. 1996, ApJ, 472, 660
Bensby, T., Yee, J. C., Feltzing, S., et al. 2013, A&A, 549, A147
Bessell, M. S., & Brett, J. M. 1988, PASP, 100, 1134
Bond, I. A., Abe, F., Dodd, R. J., et al. 2001, MNRAS, 327, 868
Cassan, A. 2008, A&A, 491, 587
Chabrier, G. 2003, PASP, 115, 763
Chung, S.-J., Gould, A., Skowron, J., et al. 2019, ApJ, 871, 179
Di Stefano, R., & Mao, S. 1996, ApJ, 457, 93
Dominik, M. 1999, A&A, 349, 108
Erdl, H., & Schneider, P. 1993, A&A, 268, 453
Gaia Collaboration (Prusti, T., et al.) 2016, A&A, 595, A1
Gaia Collaboration (Brown, A. G. A., et al.) 2018, A&A, 616, A1
Gaudi, B. S. 1998, ApJ, 506, 533
Gould, A. 1992, ApJ, 392, 442
Gould, A. 2000, ApJ, 542, 785
Gould, A., & Loeb, A. 1992, ApJ, 396, 104
Gould, A., Jung, Y. K., Hwang, K.-H., et al. 2022, JKAS, submitted, [arXiv:2204.03269]
Grether, D., & Lineweaver, C. H. 2006, ApJ, 640, 1051
Griest, K., & Safizadeh, N. 1998, ApJ, 500, 37
Han, C., & Gould, A. 2003, ApJ, 592, 172
Han, C., & Gould, A. 1995, ApJ, 447, 53
Han, C., Bond, I. A., Udalski, A., et al. 2019, ApJ, 876, 81
Han, C., Lee, C.-U., Udalski, A., et al. 2020a, AJ, 159, 134
Han, C., Kim, D., Udalski, A., et al. 2020b, AJ, 160, 64
Han, C., Udalski, A., Kim, D., et al. 2020c, A&A, 642, A110
Han, C., Lee, C.-U., Ryu, Y.-H., et al. 2021a, A&A, 649, A91
Han, C., Udalski, A., Kim, D., et al. 2021b, A&A, 655, A21
Han, C., Gould, A., Bond, I. A., et al. 2022, A&A, 662, A70
Herald, A., Udalski, A., Bozza, A., et al. 2022, A&A, 663, A100
Jung, Y. K., Udalski, A., Yee, J. C., et al. 2017, AJ, 153, 129
Jung, Y. K., Udalski, A., Gould, A., et al. 2018, AJ, 155, 219
Jung, Y. K., Han, C., Udalski, A., et al. 2021, AJ, 161, 293
Kervella, P., Thévenin, F., Di Folco, E., & Ségransan, D. 2004, A&A, 426, 29
Kim, S.-L., Lee, C.-U., Park, B.-G., et al. 2016, JKAS, 49, 37
Kim, D.-J., Kim, H.-W., Hwang, K.-H., et al. 2018a, AJ, 155, 76
Kim, H.-W., Hwang, K.-H., Shvartzvald, Y., et al. 2018b, ArXiv e-prints [arXiv:1806.07545]
Mao, S., & Paczyński, B. 1991, ApJ, 374, L37
Miyazaki, S., Sumi, T., Bennett, D. P., et al. 2018, AJ, 156, 136
Nataf, D. M., Gould, A., Fouqué, P., et al. 2013, ApJ, 769, 88
Paczyński, B. 1986, ApJ, 304, 1
Robin, A. C., Reylé, C., Derrière, S., & Picaud, S. 2003, A&A, 409, 523
Shvartzvald, Y., Yee, J. C., Skowron, J., et al. 2019, AJ, 157, 106
Skowron, J., Udalski, A., Gould, A., et al. 2011, ApJ, 738, 87
Udalski, A. 2003, Acta Astron., 53, 291
Udalski, A., Szymański, M. K., & Szymański, G. 2015, Acta Astron., 65, 1
Udalski, A., Szymański, M., Kałużny, J., et al. 1993, Acta Astron., 43, 289
Woźniak, P. R. 2000, Acta Astron., 50, 421
Yee, J. C., Shvartzvald, Y., Gal-Yam, A., et al. 2012, ApJ, 755, 102
Yoo, J., DePoy, D. L., Gal-Yam, A., et al. 2004, ApJ, 603, 139

[1] Department of Physics, Chungbuk National University, Cheongju 28644, Republic of Korea
e-mail: cheongho@astroph.chungbuk.ac.kr
[2] Korea Astronomy and Space Science Institute, Daejon 34055, Republic of Korea
[3] Department of Earth and Space Science, Graduate School of Science, Osaka University, Toyonaka, Osaka 560-0043, Japan
[4] Dipartimento di Fisica "E. R. Caianiello", Universitá di Salerno, Via Giovanni Paolo II, 84084 Fisciano SA, Italy
[5] Istituto Nazionale di Fisica Nucleare, Sezione di Napoli, Via Cintia, 80126 Napoli, Italy
[6] University of Canterbury, Department of Physics and Astronomy, Private Bag 4800, Christchurch 8020, New Zealand
[7] Department of Astronomy, Tsinghua University, Beijing 100084, PR China
[8] Astronomical Observatory, University of Warsaw, Al. Ujazdowskie 4, 00-478 Warszawa, Poland
[9] Institute of Natural and Mathematical Science, Massey University, Auckland 0745, New Zealand
[10] Max-Planck-Institute for Astronomy, Königstuhl 17, 69117 Heidelberg, Germany
[11] Department of Astronomy, Ohio State University, 140 W. 18th Ave., Columbus, OH 43210, USA
[12] Department of Particle Physics and Astrophysics, Weizmann Institute of Science, Rehovot 76100, Israel
[13] School of Space Research, Kyung Hee University, Yongin, Kyeonggi 17104, Republic of Korea
[14] Korea University of Science and Technology, Korea, (UST), 217 Gajeong-ro, Yuseong-gu, Daejeon 34113, Republic of Korea
[15] Center for Astrophysics, Harvard & Smithsonian, 60 Garden St., Cambridge, MA 02138, USA
[16] Department of Physics, University of Warwick, Gibbet Hill Road, Coventry CV4 7AL, UK
[17] Institute for Space-Earth Environmental Research, Nagoya University, Nagoya 464-8601, Japan
[18] Code 667, NASA Goddard Space Flight Center, Greenbelt, MD 20771, USA
[19] Department of Astronomy, University of Maryland, College Park, MD 20742, USA
[20] Department of Earth and Planetary Science, Graduate School of Science, The University of Tokyo, 7-3-1 Hongo, Bunkyo-ku, Tokyo 113-0033, Japan
[21] Instituto de Astrofísica de Canarias, Vía Láctea s/n, 38205 La Laguna, Tenerife, Spain
[22] Department of Physics, The Catholic University of America, Washington, DC 20064, USA
[23] Department of Astronomy, Graduate School of Science, The University of Tokyo, 7-3-1 Hongo, Bunkyo-ku, Tokyo 113-0033, Japan
[24] Zentrum für Astronomie der Universität Heidelberg, Astronomisches Rechen-Institut, Mönchhofstr. 12-14, 69120 Heidelberg, Germany
[25] Department of Physics, University of Auckland, Private Bag 92019, Auckland, New Zealand
[26] University of Canterbury Mt. John Observatory, PO Box 56, Lake Tekapo 8770, New Zealand